GSA Data Repository item 2017091

Supplementary Material for

Block-controlled hillslope form and persistence of topography in rocky landscapes
By Rachel C. Glade, Robert S. Anderson, and Gregory E. Tucker

I) Detailed field methods and locations

II) Detailed numerical modeling methods

III) We present additional model runs and discussion that serve 1) to demonstrate that the results are insensitive to the details of the chosen soil production algorithm, 2) to amplify our argument that it is the blocks that matter in the development of these landforms, 3) to explore the influence of select parameters, including initial spatial block distributions and relative weathering rates.

IV) Animation of model (see video in GSA Data Repository item 2017091).

I) Field methods

a) Topographic profiles in Fig. 1b

Topographic profiles were collected from Google Earth using the elevation profile tool. Profiles were chosen in locations that lack evidence of significant human influence or drainage networks and were drawn perpendicular to the strike of the resistant layer. Profiles were not preferentially selected on concave-up slopes, and start just beyond the slope break at the base of the slope. Hogbacks in the eastern United States and Europe were discounted due to extreme human influence.

Location	Latitude	Longitude
Colorado, US	40.458363	-105.199208
Colorado, US	40.312157	-105.239943
Colorado, US	40.547748	-105.165826
Colorado, US	40.725025	-105.183402
Colorado, US	40.699388	-105.184904
Colorado, US	39.639511	-105.183131
Wyoming, US	42.701353	-106.189737
Eastern Cape, South Africa	-32.733672	26.965292
Eastern Cape, South Africa	-32.705649	27.045712
Magaliesberg, South Africa	-25.793916	27.651946
Montana, US	45.407226	-112.582343
Victoria, Australia	-37.601315	142.354860
Victoria, Australia	-37.190382	142.567758
Victoria, Australia	-37.158089	142.539663
Carazo, Spain	41.995733	-3.413723

Table DR1. Coordinates of topographic profiles derived from Google Earth

b) Topographic profile in Fig. 2a

Topographic profile was obtained from 1-m resolution LiDAR from Boulder Creek Critical Zone Observatory August 2010 Snow-Off LiDAR Survey collected 8/21/2010-8/26/2010**.** Data is available online at OpenTopo.sdsc.edu/datasets. Profile coordinates are 40.148693 N, -

105.295822 W. Figure DR1 shows additional profiles from Heil Valley Ranch, as well as slope values.

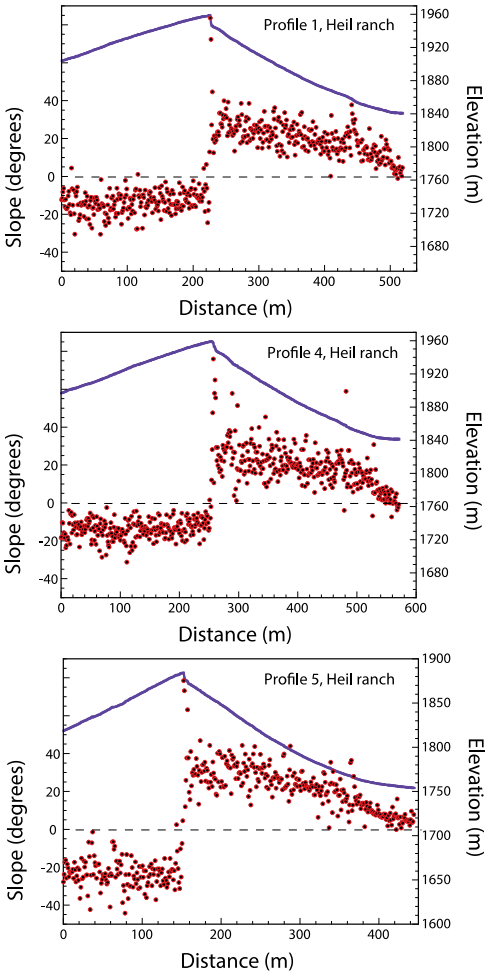

Fig. DR1 Elevation profiles and trends in slope derived from 1-meter resolution LiDAR data of hogbacks adjacent to the Front Range, Colorado. The magnitude of the slope declines with distance downhill from the top of the ramp.

c) Field work

i) Block size

We conducted field work at Heil Valley Ranch Open Space, north of Boulder, Colorado. The profile begins at 40.152270 N, -105.296935 W**.** Data was collected at 10 sites along a profile running perpendicular from the crest. Each site was 100 square meters, and spaced 30 meters apart. At each site we counted every block over 10 cm in diameter; we also chose at random 10

blocks and measured the surface-parallel long and short axis. The third axis was not measured due to partial burial of the blocks by soil or pine needles. Block size data are shown in Table DR2.

Site #	**Site 1**		**Site 2**		**Site 3**		**Site 4**		**Site 5**		**Site 6**		**Site 7**		**Site 8**		**Site 9**		**Site 10**	
Size	**L**	**W**	**L**	**W**	**L**	**W**	**L**	**W**	**L**	**W**	**L**	**W**	**L**	**W**	**L**	**W**	**L**	**W**	**L**	**W**
[m]	1.1	1.1	1.0	0.6	1.4	0.9	0.5	0.3	0.7	0.5	0.6	0.5	1.4	0.7	4.0	3.0	0.7	0.3	0.8	0.8
	0.4	0.3	0.5	0.2	0.4	0.3	0.5	0.3	0.5	0.3	5.0	4.0	1.1	0.8	3.0	1.0	0.7	0.5	1.1	0.4
	1.0	0.9	1.2	0.5	0.4	0.3	0.4	0.2	0.4	0.3	4.0	3.0	1.0	0.8	1.0	1.0	1.0	0.5	4.0	2.0
	0.4	0.2	0.4	0.3	1.0	0.9	1.5	0.9	2	1.4	0.7	0.4	3.0	2.0	1.0	0.6	1.0	0.6	0.4	0.2
	0.4	0.2	0.4	0.3	1.4	1.3	0.7	0.5	0.3	0.3	0.7	0.6	2.0	1.5	1.5	0.8	0.3	0.3	0.8	0.4
	0.5	0.3	0.4	0.3	0.9	0.5	3.4	2.0	1.2	0.6	2.0	1.6	0.5	0.4	0.8	0.6	5.0	2.0	0.9	0.2
	0.2	0.15	0.9	0.5	0.3	0.2	0.4	0.3	0.4	0.3	0.9	0.4	2.0	2.0	1.5	1.0	0.5	0.5	3.5	2.0
	0.7	0.7	1.5	0.9	0.8	0.5	0.4	0.3	0.7	0.5	0.3	0.2	0.8	0.6	1.2	1.2	0.3	0.3	5.0	2.0
	0.35	0.2	0.4	0.35	0.6	0.5	0.9	0.4	1.2	0.6	0.6	0.4	0.7	0.6	3.0	1.2	0.9	0.4	0.6	0.5
	0.2	0.1	0.3	0.3	1.0	0.7	0.4	0.3	0.9	0.8	1.4	1.0	0.8	0.3	0.5	0.4	0.9	1.2	0.8	0.4
SEM	0.0735		0.0785		0.0840		0.1724		0.1724		0.3263		0.1600		0.2246		0.2350		0.3045	

Table DR2. Block size data from Heil Valley Ranch, Boulder, Colorado. L (length) values represent the longer of two axes measured. W (width) values represent shorter axis measured. Values have units of meters. Site numbers begin at base of slope (Site 1) and increase in elevation.

ii) Schmidt Hammer

For each of 10 blocks at each field site, we collected 15 Schmidt Hammer (Type N) measurements, totaling 150 Schmidt hammer measurements per site. This is well above the suggested number of Schmidt hammer readings for sandstone (Niedzielski et al., 2009). While blocks were derived from a constant resistant layer of Dakota Sandstone, a small number of blocks were composed of a conglomerate; these were removed from the Schmidt Hammer data, since the absence of a flat surface from which to collect measurements biases the Schmidt Hammer to give low readings. At sites where this occurred, calculation of standard error incorporated the smaller sample size; however, sample size always remained greater than the

number suggested by Niedzielski et al., 2009. See Table DR3 for complete Schmidt hammer data.

Site #	Site 1		Site 2		Site 3		Site 4		Site 5		Site 6		Site 7		Site 8		Site 9		Site 10	
Rebound	M	S	M	S	M	S	M	S	M	S	M	S	M	S	M	S	M	S	M	S
Value	28.9	14.2	45.1	7.4	42.0	10.2	58	11.6	36.3	17.5	56.4	7.7	56	10.1	59.5	6.4	57	8.6	48.5	12.1
Mean (M)	51.7	15.9	45.1	6.8	49.2	9.8	37	17.1	55.8	12.3	46.8	12.5	59.2	7.9	37.7	8.6	39.5	13.3	63.3	7.2
St. Dev (S)	34.6	17.3	45.1	13.1	66.7	6.3	57.7	11.8	52.7	10.3	52.6	9.4	54	9.8	59.4	7.8	57.9	13.8	59.6	4.8
	42.5	8.3	47.9	6.8	53.7	10.1	59.1	4.3	50	14.4	61.7	11.6	41	13.5	59	5	54.2	9.1	54.8	10.7
	45.4	9.8	46.3	11.5	36.2	14.5	58.8	9.8	54.1	8.7	59.1	9.4	45.9	13.8	61.6	7.3	55.2	13.6	58.9	11.6
	27.5	9.9	52.1	7.7	35.8	16.4	46.4	10.3	53.9	10.6	49.2	14.5	57.1	7.3	60.4	5.6	66.3	7.6	54.9	14.7
	25.9	10.5	47.6	10.3	47.6	13	41.7	13.2	61.1	6.4	58.5	7.9	54.9	11.8	35.2	10	60.9	2.9	36.8	13.1
	61.4	6.9	30.8	8.6	32.3	9	52.4	8.8	36.8	13.8	57.8	12.1	57.8	7.8	48.2	8.4	63.6	8.3	40.8	13.9
	48.2	16.6	35.9	13.8	58.9	10.5	55.7	9.6	57.4	6.5	53.4	7.1	51.3	13	48.8	10.9	64.2	6.7	47.3	18.1
	42.4	10.7	64.8	5.6	59.6	7.9	56.9	6.3	59.9	6.5	51.7	13.3	53.5	9.5	57.5	10.7	60.8	6.2	43.6	12.6
St. Dev	16.6		15.1		15.2		10.2		10.5		9.9		10.1		9.4		9.9		10.9	
SEM	1.4		1.2		1.2		0.8		0.9		0.8		0.8		0.8		0.8		0.9	

Table DR3. Schmidt Hammer rebound values. Columns show mean (M) rebound value and standard deviation (S), for each block (each mean and standard deviation is composed of 15 individual measurements). Combined standard deviation and SEM for each site is reported in the bottom rows. Site numbers begin at base of slope (Site 1) and increase in elevation. Red values show blocks of conglomerate lithology, which were not included in final mean, st. dev or SEM calculations due to biased readings (see text above).

When using the Schmidt Hammer, it is possible that measurements may be biased due to size effects of the blocks; small block may give artificially low readings, especially when measurements are taken too close to cracks or edges (Sumner and Nel, 2002; Demirdag et al., 2009). To explore whether this effect biases our data, we plot Schmidt Hammer rebound value for each block against that block's mean size (Fig. DR2) and length of the shortest axis (Fig. DR3). The lack of a positive trend in either plot assures us that block size does not skew the Schmidt Hammer results; that is, the decrease in Schmidt Hammer rebound values is not simply an artefact of decreasing block size.

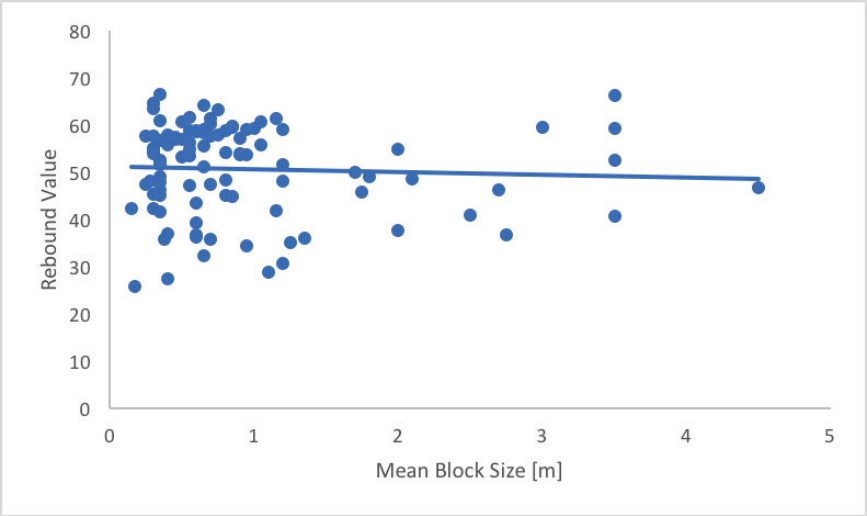

Fig. DR2. Comparison of Schmidt Hammer rebound value with mean block size for each measured block (the mean of measured long and short axes).

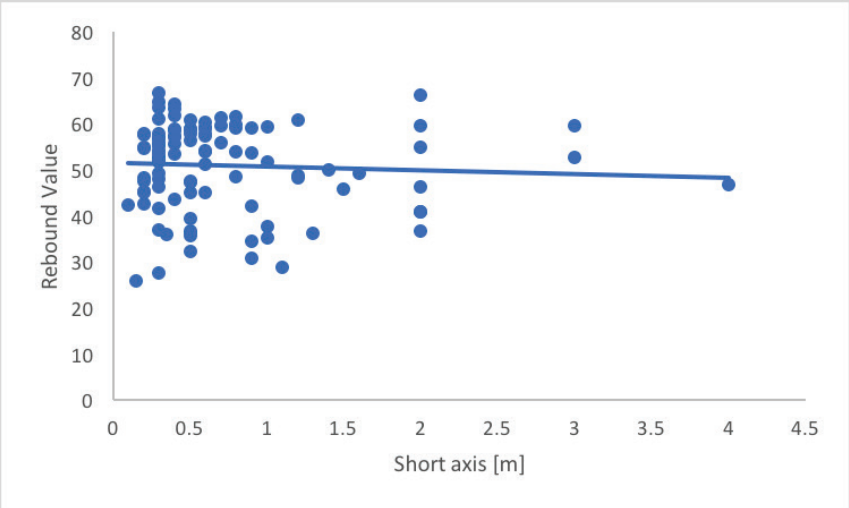

Fig. DR3. Comparison of Schmidt Hammer rebound value with short axis length for each measured block.

The Schmidt Hammer data presented in Fig. 2 of the main text displays a pronounced decrease in rebound values beginning around 200 meters from the crest. At this point, both mean rebound values and mean block size decrease abruptly. This could be an indication of a shift from dominantly physical weathering processes to dominantly chemical weathering processes. Schmidt Hammer rebound values can be used as a proxy for chemical weathering in sandstone (Tugrul, 2004), but do not respond to physical or mechanical breakdown or rocks. Therefore, we posit that the relatively constant (with a slight decrease) in rebound values over the first 200 m represents the dominance of mechanical weathering or splitting of blocks over a smaller chemical weathering component, whereas the rapid decrease in rebound values beyond 200 m represents a shift to dominantly chemical weathering. A potential mechanism for this shift is a change in efficiency of thermally-induced cracking. Field experiments have shown that thermally induced cracking of rocks can be an efficient process of mechanical weathering of large blocks (Eppes et al., 2016). However, the efficiency of cracking due to thermal stresses has been shown to decrease with decreasing block size (Aldred et al., 2015). Further work is needed to test this hypothesis. At present we suggest that it is a plausible explanation for the trend in Schmidt Hammer data in Figure 2.

II) Modeling methods

The numerical model links algorithms for block release, mobile regolith (soil) production by weathering, and both soil and block transport. The governing equations are discretized and solved using an Euler forward finite difference scheme.

Block release and placement

Joints are assumed to be oriented perpendicular to the dip of the resistant layer. Joint-bounded blocks are released from the resistant layer when the elevation drop between the edge of the hard layer and the shale slope is:

$$z(r) - z(s) = D/sin\beta \quad (3)$$

where $z(r)$ is the elevation of the base of the resistant layer at its edge, $z(s)$ is the elevation of the shale slope immediately beneath the resistant layer, D is the thickness of a block (or the distance between joints) and β is the dip of the resistant layer. Blocks are deposited on the shale ramp immediately adjacent to the resistant layer, one in each cell. The number of blocks to be placed

depends on the thickness of the jointed layer and the specified block size. See Fig. DR4 for an illustration of equation 3.

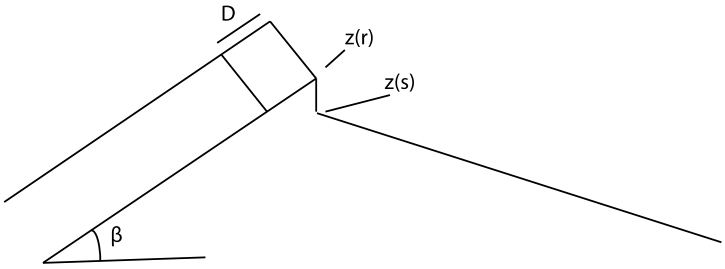

Fig. DR4. Definition sketch of parameters relevant to block release in Eq. 3.

Block weathering

Weathering, or here the conversion of bedrock to soil by any process, is represented as a function of depth to the soil-bedrock interface. We use an equation for weathering rate that can accommodate both an exponential rule and a rule in which soil production is maximized at some finite depth (the so-called "humped" weathering rule):

$$w = w_0 e^{-H/H_w} + w_1 \frac{H}{H_w} e^{-H/H_w} \quad (4)$$

The first term represents a simple exponential decline with soil thickness, with a bare bedrock rate, w_o, and a characteristic soil depth H_w at which the bedrock conversion rate has declined to 1/e of that on bare bedrock. The second term is a gamma function with a peak at $H=H_w$ and a peak of w_1. We capture the pure exponential case by setting $w_1=0$.

We honor the difference between the two bedrock types in the model by specifying a ratio of the bare bedrock weathering rates, w_{0shale} and $w_{0sandstone}$ (e.g., $w_{0shale}/w_{0sandstone} = 100$). Blocks weather vertically according to Eq. (4), using $w_{0sandstone}$. Therefore, blocks weather in the same manner as the shale, but more slowly. Any soil buildup on top of the blocks contributes to a lowering of block weathering rate according to Eq. (4). Soil thickness under each block is maintained until the block moves.

Soil transport

Our algorithm for downslope discharge of soil, q [=] L^3/LT, honors the dependence on slope and on soil thickness. Here we cast the dependence as

$$q = -kSh_* \left(1 - e^{-\frac{H}{h_*}}\right) \qquad (5)$$

where k is a soil transport efficiency or here a characteristic velocity with units of L/T, S the local slope, H the local soil thickness, and h^* a characteristic soil thickness representing the depth scale of any particular transport process (Anderson, 2002; Johnstone and Hilley, 2015). The first factor captures a simple flux dependence on slope. The term in brackets assures that transport vanishes at zero soil thickness: as H/h_* approaches zero, soil discharge vanishes. At the other end-member of thick soil, $H/h_* >> 1$, transport becomes insensitive to soil thickness and is governed instead simply by the local slope. The use of a linear flux law ensures that any non-convex hillslope form generated by the model can be attributed to the presence of blocks, and is not the result of a non-linear flux law.

Block movement

Blocks may move downslope only when sufficient relief exists. This will evolve as soil is transported away from the cell immediately downslope of a block. We define a threshold for block motion in which a block will move one cell downhill if relief is greater than or equal to twice the current height of a block. Therefore, as blocks weather and their size decreases, they move more easily. This choice of rule for block movement is simply a parameterization; more work is needed to understand the specific processes that allow blocks to move downslope, which may include toppling or sliding. However, setting a relief threshold for movement in the model essentially asserts that blocks are more likely to move when the local slope is steeper; this is likely to be a valid parameterization regardless of the specific transport method.

Boundary conditions

We specify an elevation history on each lateral boundary of the calculation space, representing incision of local streams. We present results for constant river incision, which is required for the system to reach a steady state form. Here we choose channel incision rate to be 5×10^{-5} m/yr.

Comparison of analytical and numerical models

The slope is reported for every 10-m increment of the ramp in the numerical model, beginning at 15 meters from the peak where the slope is not affected by initially placed blocks. For comparison with the analytic model, we also report the analytical slope (eqn. 2) using the mean block size (D), spacing (X_s), and the soil production rate (w), for the same 10-m increments. We use mean weathering rate from the model, which accounts for the lower weathering rate of the blocks. As we employ the soil depth-dependent flux law (Eq. 5) in the numerical model, we also incorporate the depth-dependent term in the analytical solution for the comparison shown in Figure 4.

III) Additional model runs

Comparison of models with exponential vs. humped soil production rules

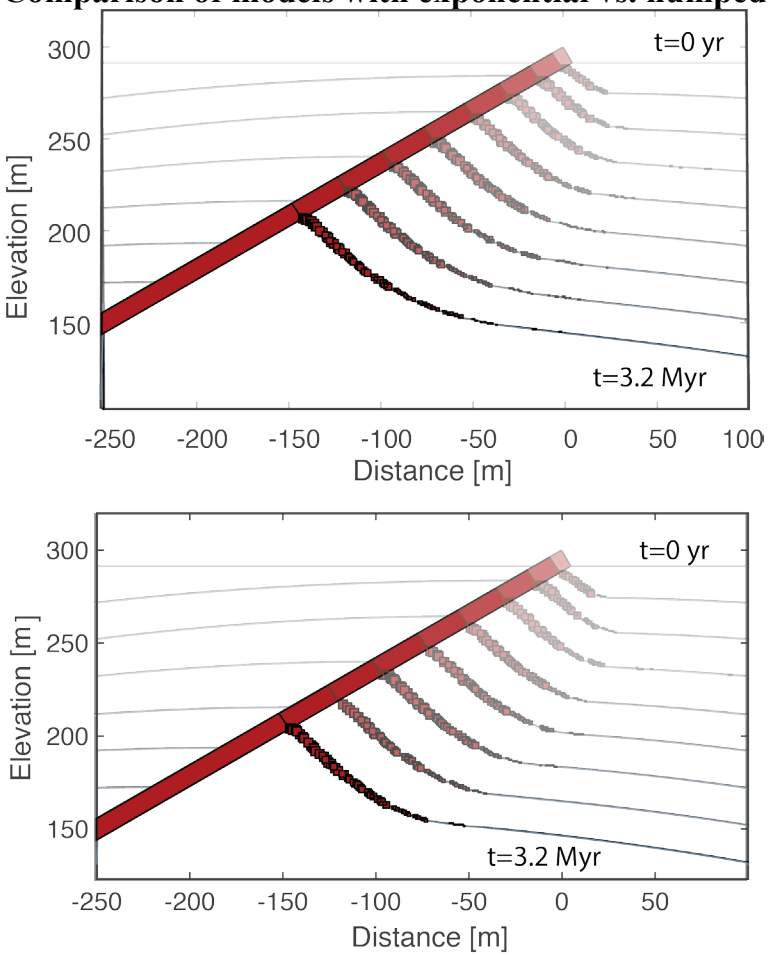

Fig. DR5. Comparison of model using exponential soil production rule employed in the main text (top) with model using humped soil production rule (bottom) (following Anderson and Humphrey, 1989, and Mudd and Furbish, 2007). Both runs employ a bare bedrock weathering rate of $1x10^{-5}$ m/yr for the resistant layer, and $1x10^{-3}$ m/yr for the shale. For the humped soil production rule (see methods Eq. 4) we set w_1=$1x10^{-4}$ m/yr. Differences between model runs are subtle, and do not substantially alter the conclusions: both rules result in concave ramps with significant relief.

Comparison of block model with control run

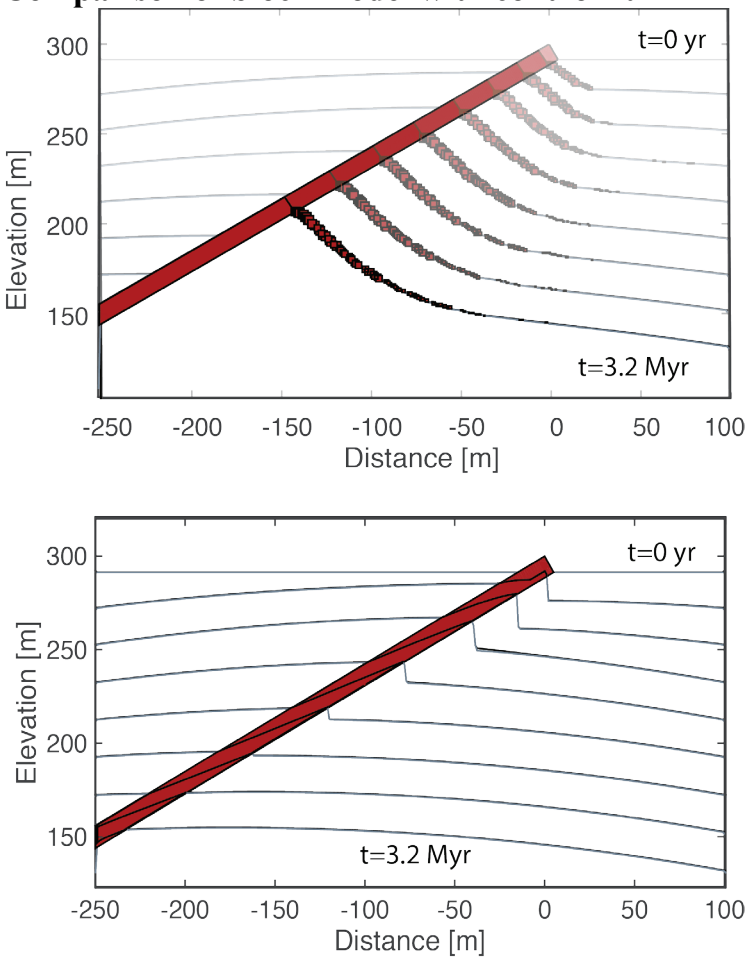

Fig. DR6. Comparison of numerical model presented in the text (top) with control model in which blocks are not included (bottom). Models share the same boundary conditions, a constant lowering rate of $5x10^{-5}$ m/yr. The control run employs a bare bedrock soil production rate of $1x10^{-5}$ m/yr for the resistant layer (red), and $1x10^{-3}$ m/yr for the shale. An initial steep cliff develops due to the difference in soil production rates, but the step declines over time, resulting in a parabolic profile with an offset along the hard layer. Slopes in the control run are purely convex, as expected in steady state diffusive systems. The difference between the model runs illustrates the importance of blocks in creating concave slopes rather than convex, and in maintaining significant relief. Relief in the control run is approximately 60 m smaller than that in the model with blocks.

Initial block placement

The numerical model presented in the main text assumes that blocks released from the resistant layer are deposited a short distance away from the cliff. We argue that this simplified view is a good approximation for hogbacks with a relatively thin resistant layer, where blocks are back-tilted and do not have much vertical distance to fall before landing on the slope below. However, hogbacks, mesas, or other scarps may have substantial relief between the resistant layer and the

adjoining slope, allowing for further initial transport of the blocks. Here we compare the original model presented in the main text (Fig. DR7) with two modified model outputs that include further initial transport distance of blocks immediately after release. Figure DR8 shows a model run in which blocks are deposited immediately downslope of the cliff, but with 1 model cell in between each block. This does not substantially alter the first-order results. Figure DR9 shows a model run in which blocks have a probability of being initially placed far from the crest according to a truncated normal distribution. This allows most blocks to be deposited near the crest, while some blocks have the opportunity to travel much further. This also does not substantially alter the first-order effects; however, the trend in block size downslope is more scattered, due to stochasticity. Further work is needed to quantify the effects of different initial block placement distributions.

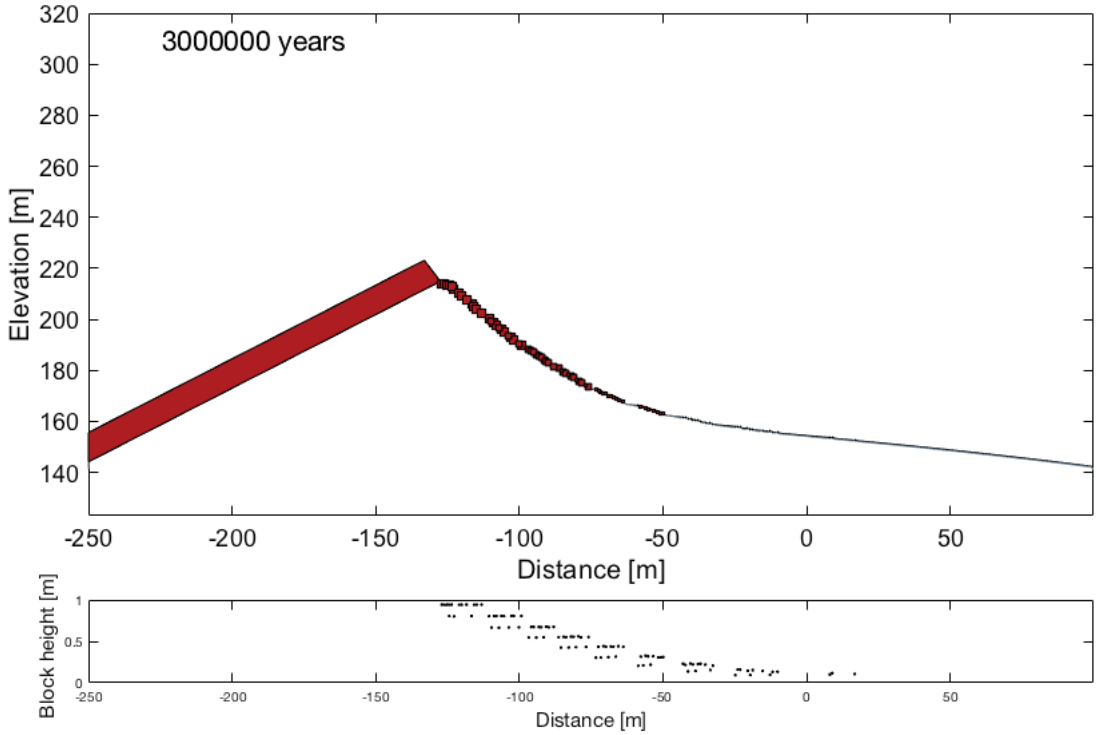

Fig. DR7. Original numerical model results, presented in main paper. Lower subset shows block size distribution.

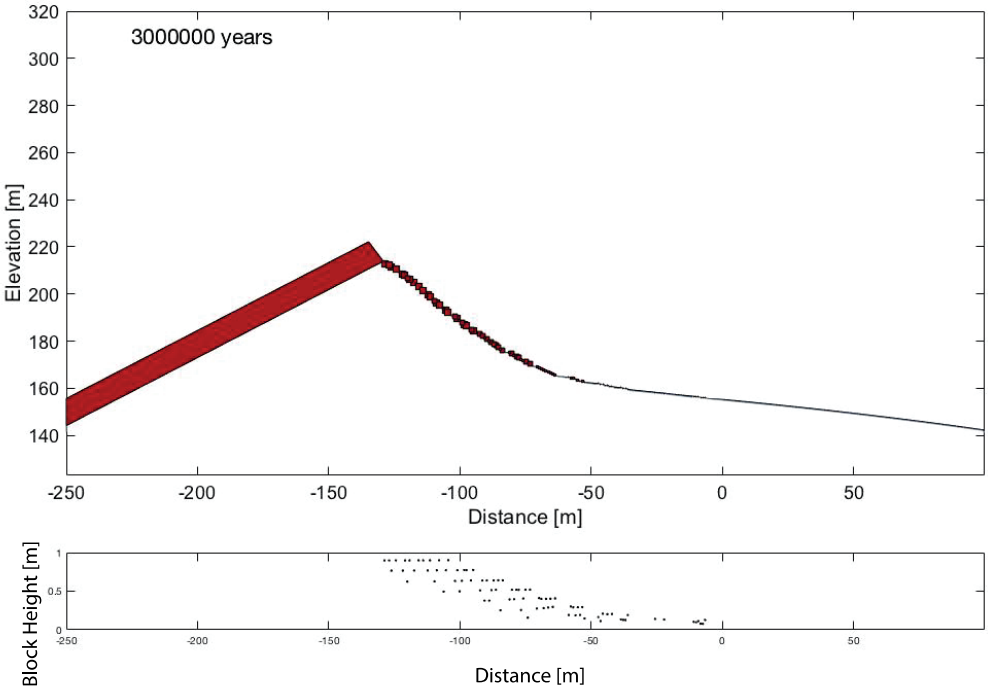

Fig. DR8. Model output for initial block placement beginning immediately downslope of the crest with 1 model cell in between each block. All other parameters are identical to model output presented in main paper. Lower subset shows block size distribution.

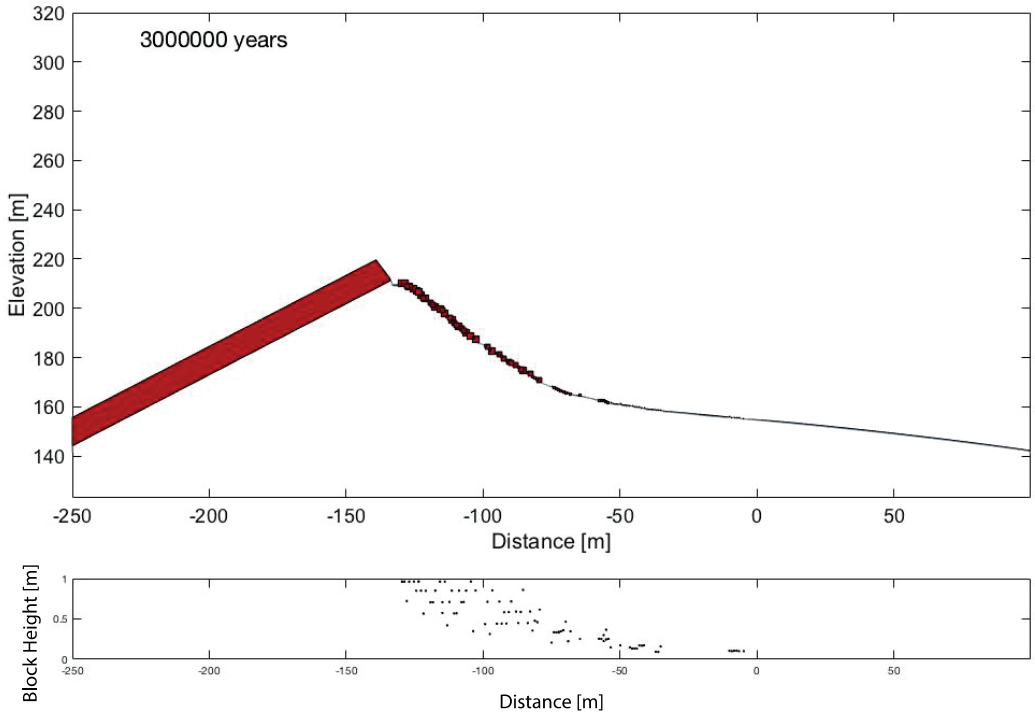

Fig. DR9. Model output for initial block placement with a truncated normal distribution, using a standard deviation of 20 meters from the crest. All other parameters are identical to model output presented in main paper. Lower subset shows block size distribution.

Relative Weathering Rates

Here we briefly explore the effect of changing the ratio between the maximum weathering rate of the blocks and that of the underlying shale. Results presented in the main paper show a hogback in which the weathering rate of the blocks is 100 times lower than that of the shale. Fig. DR10 shows that when blocks have a weathering rate that is 50 times lower than that of the shale, the resulting concave-up slope is shorter in both length and relief. Conversely, Fig. DR11 shows that when the weathering rate of the blocks is 1000 times lower than that of the shale, the resulting slope is much greater in both length and relief.

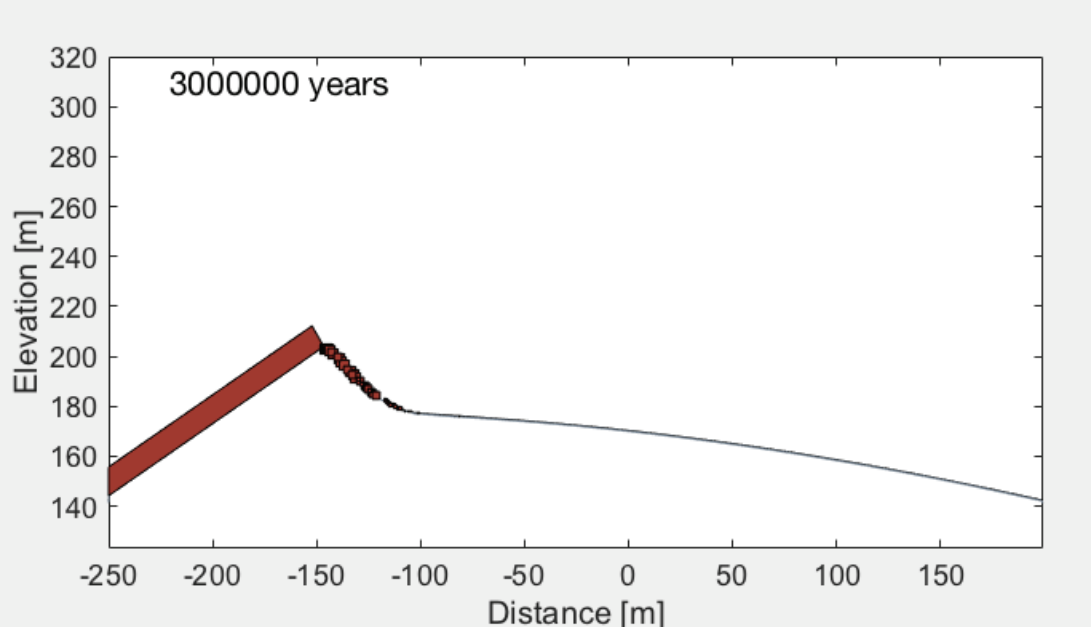

Fig. DR10. Model output for a relatively low contrast between weathering rates of blocks and underlying shale (weathering rate of blocks is 50 times lower than that of shale). Resulting block-covered slope is shorter in length and relief than results in main paper.

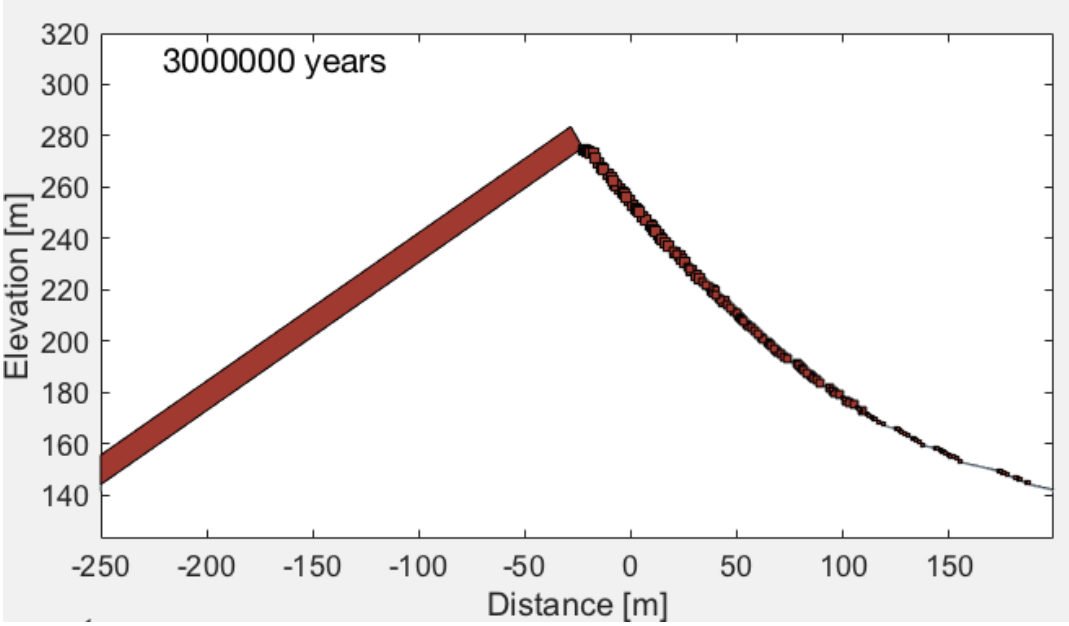

Fig. DR11. Model output for a relatively high contrast between weathering rates of blocks and underlying shale (weathering rate of blocks is 1000 times lower than that of shale). Resulting block-covered slope is greater in length and relief than results in main paper.

Supplementary References

Aldred, J., Eppes, M.C., Aquino, K., Deal, R., Garbini, J., Swami, S. Tuttle, A. and Zanthos, G., 2015, The influence of solar-induced thermal stresses on the mechanical weathering of rocks in humid mid-latitudes: Earth Surf. Process. Landf., v. 41, p. 603-614.

Anderson, R.S., and Humphrey, N.F., 1989, Interaction of weathering and transport processes in the evolution of arid landscapes, in: T. Cross (ed.), Quantitative Dynamic Stratigraphy, Englewood Cliff, NJ: Prentice-Hall, pp. 349–361.

Anderson, R.S., 2002, Modeling of tor-dotted crests, bedrock edges and parabolic profiles of the high alpine surfaces of the Wind River Range, Wyoming: Geomorphology v. 46, p. 35-58.

Demirdag, S., Yavuz, H., and Altindag, R., 2009, The effect of sample size on Schmidt rebound hardness value of rocks: International Journal of Rock Mechanics and Mining Sciences, v. 46, p. 725-730.

Eppes, M.C., Magi, B., Hallet, B., Delmelle, E., Mackenzie-Helnwein, P., Warren, K. and Swami, S., 2016, Deciphering the role of solar-induced thermal stresses in rock weathering: GSA Bulletin, v. 128, p. 1315-1338.

Johnstone, S.A., and Hilley, G.E., 2015, Lithologic control on the form of soil-mantled hillslopes: Geology, v. 43 (1), 1–5, doi:10.1130/G36052.1.

Mudd, S.M. and Furbish, D.J., 2007, Responses of soil-mantled hillslopes to transient channel incision rates: Journal of Geophysical Research – Earth Surface v. 112, F03S18, doi: 10.1029/2006JF000516.

Niedzeilski, T., Migoń, P. and Placek, A., 2009, A minimum sample size required from Schmidt hammer measurements: Earth Surf. Process. Landf., v. 34, p. 1713-1725.

Sumner, P. and Nel, W., 2002, The effect of tock moisture on Schmidt hammer rebound: tests on rock samples from Marion Island and South Africa: Earth Surf. Process. Landf., v. 27, p. 1137-1142.

Tugrul, A, 2004, The effect of weathering on pore geometry and compressive strength of selected rock types from Turkey: Eng Geol, v. 75, p. 215-227.